Materials Science Forum
ISSN: 1662-9752, Vol. 1175, pp 129-134
doi:10.4028/p-1D1HhB

Submitted: 2025-07-23
Revised: 2025-09-05
Accepted: 2025-10-28
Online: 2026-01-16

Influence of Hierarchical Structure on Mechanical Properties of Additive Manufactured IN718 Alloys

Kippei Yamashita[1,a*], Ken Cho[1,2,b], Takuma Saito[3,c], Taisuke Sasaki[3,d], Katsuhiko Sawaizumi[1,e], Masayuki Okugawa[1,2,f], Yuichiro Koizumi[1,2,g], Takayoshi Nakano[1,2,h] and Hiroyuki Y. Yasuda[1,2,i]

[1]Division of Materials and Manufacturing Science, Graduate School of Engineering, The University of Osaka, 2-1, Yamadaoka, Suita, Osaka 565-0871, Japan

[2]Anisotropic Design & Additive Manufacturing Research Center, Graduate School of Engineering, The University of Osaka, 2-1, Yamadaoka, Suita, Osaka 565-0871, Japan

[3]Research Center for Magnetic and Spintronic Materials, National Institute for Materials Science, 1-2-1, Sengen, Tsukuba, Ibaraki 305-0047, Japan

[a]kippei.yamashita@mat.eng.osaka-u.ac.jp, [b]k_cho@mat.eng.osaka-u.ac.jp, [c]Takuma.Saito@ruhr-uni-bochum.de, [d]SASAKI.taisuke@nims.go.jp, [e]katsuhiko.sawaizumi@mat.eng.osaka-u.ac.jp, [f]okugawa@mat.eng.osaka-u.ac.jp, [g]ykoizumi@mat.eng.osaka-u.ac.jp, [h]nakano@mat.eng.osaka-u.ac.jp, [i]hyyasuda@mat.eng.osaka-u.ac.jp

Keywords: Nickel-based superalloy, Selective laser melting, Crystallographic texture, Cellular structure, Hardening mechanism

Abstract. Selective laser melting (SLM) can produce Ni-based superalloys with a unique hierarchical structure consisting of micrometer-scale crystallographic lamellar microstructure and nanometer-scale cellular structure under optimized process parameters. This work investigated the effects of input energy density on the morphology of the cells and its influence on the tensile properties of Ni-based superalloy prepared by SLM. We found that the cell spacing decreases with decreasing input energy density. Further investigation of the cells clarified that the boundary of cells is a low angle grain boundary with dislocation cell wall and segregation of certain elements such as Nb and Ti. Moreover, it was demonstrated that the boundary of cells performs as a significant barrier to the griding dislocation. Thus, the cell boundary leads to strong strengthening through the Hall-Petch law.

Introduction

Ni-based superalloys have been used for the aerospace and energy industries due to their outstanding high-temperature strength and grate oxidation resistance [1]. In particular, the great mechanical properties of practical Ni-based superalloys (e.g., Inconel 718 and Hastelloy X) are mainly attributed by precipitations such as the γ' ($L1_2$ structure: $Ni_3(Al, Ti)$) and γ'' ($D0_{22}$ structure: Ni_3Nb) phases within the γ matrix (face-centered cubic (fcc) structure) [2]. In general, Inconel 718 parts are fabricated by casting, wrought or powder metallurgy methods [3]. On the other hand, Inconel 718 exhibits poor machinability at room temperature because of its high strength and low thermal conductivity.

To address this problem, metal additive manufacturing (MAM) has attracted significant attention as a promising process for manufacturing Inconel 718 parts. Powder bed fusion (PBF), one of the most successful MAMs, is an effective process for producing structural materials and heat-resistant alloys [4-10]. Therefore, numerous studies on Inconel 718 prepared via laser PBF (SLM) have been conducted focusing on accurate defect-free building and post heat treatment to optimize the microstructure [11,12]. Gokcekaya et al. reported that unique hierarchical structure consisting of micrometer-scale crystallographic lamellar microstructure (CLM) and nanometer-scale cellular structure can be obtained in Inconel 718 fabricated by SLM under the optimized process parameters and scanning strategy [13]. The CLM is composed of single-phase layered grains with different crystallographic orientations, where main and sub-layers are parallel to <011> and <001> orientations,

respectively, in respect of the building direction (BD). In addition, the cells are a primary dendrite arm which is elongated along the preferential solidification direction. It was also revealed that Inconel 718 with the cells exhibits significantly higher strength than conventional wrought alloy even without the formation of precipitation phases such as the γ' and γ" phases [13]. However, the relationship between process parameters and the morphology of the cells has not been clarified. Furthermore, the relationship between the morphology of cells and mechanical properties is also not yet fully understood. Therefore, in this study, the characteristics of the cells and mechanical properties of the Inconel 718 fabricated by LBPF were investigated focusing on the influence of the input energy density.

Experimental

Inconel 718 raw powder prepared by Ar-gas atomization was used for fabrication. Its average diameter is approximately 30 μm. Rectangular samples (10 × 10 × 30 mm) were built using EOS M290. Three process parameters used in the present study are showed in Table 1. It is noted that the sccanning speed (v) was varied from 1000 mm/s to 1400 mm/s, while laser power (P), layer thickness (t) and hatch spacing (d) were fixed at 360 W, 0.060 mm and 0.080 mm, respectively. The input energy density (E) for each process condition was calculated according to Eq. 1.

$$E = \frac{P}{vhd}. \tag{1}$$

Hereafter, the samples fabricated under the process parameters with E values of 75.0, 62.5 and 53.6 J/mm^3 are referred to as HE, ME, and LE samples, respectively. A laser beam irradiated from Yb-fiber laser was scanned meanderingly onto every layer along X axis (scan direction, SD) (Fig. 1).

The microstructure was observed by a scanning electron microscope (SEM), a transmission electron microscope (TEM) and a scanning TEM (STEM). TEM observations were conducted at an accelerating voltage of 300 kV, whereas STEM observations were performed at 200 kV. In addition, crystallographic orientations were analyzed by an electron backscattered diffraction (EBSD) detector. These observations were carried out to the specimens taken from the center of samples using an electro discharge machine.

The tensile strength of samples was investigated using an Instron-type testing machine. The tensile tests were carried out with an initial strain rate of 1.7×10^{-4} s^{-1} at room temperature in air. The specimens were cut from the center of sample employing electro discharge machining. Its gauge dimensions of specimens were 5.0 × 1.5 × 0.5 mm. The loading axis was set parallel to the BD.

Table 1 Process parameters used in this work.

	Laser power, P [W]	Scanning speed, v [mm/s]	Layer thickness, t [mm]	Hatch spacing, d [mm]	Energy density, E [J/mm^3]
HE rod	360	1000	0.060	0.080	75.0
ME rod	360	1200	0.060	0.080	62.5
LE rod	360	1400	0.060	0.080	53.6

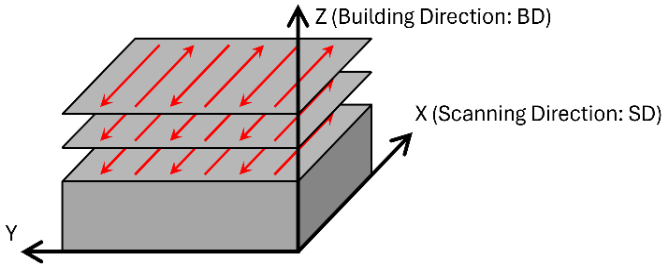

Fig. 1 Schematic drawing of scanning strategy.

Results and Discussion

Microstructures. Fig. 2 shows Z-projection of inverse pole figure (IPF) map (a) and SEM-backscattered electron (BSE) image (b) of HE sample taken from the SD. It should be noted that melt pool boundaries are indicated by dots lines. CLM, which consists of the <011>-oriented main layers and the <001>-oriented sub-layers in the respect of the BD, can be recognized in the sample. The mean widths of the A and B layers were found to be approximately 55 μm and 25 μm, respectively. The formation of CLM is observed on all samples, irrespective of the value of *E*. In addition, the width of each layer is found to be independent of *E*. As mentioned in detail in previous work, the <001>-oriented preferential solidification and the shape of the melt pool are the key factors in the formation of CLM [13].

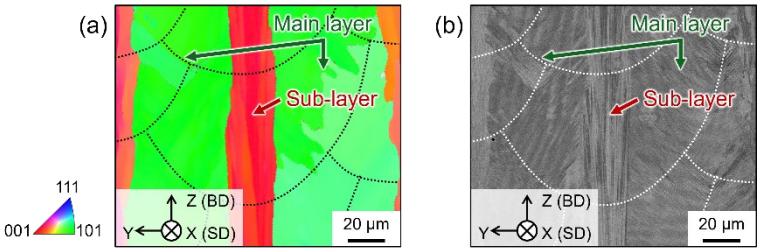

Fig. 2 Z-projection of IPF map (a) and SEM-BSE image (b) of HE rod taken from the SD.

Fig. 3 shows enlarged SEM-BSE images of the sub-layer in HE (a), ME (b) and LE (c) samples. Fine cells aligned to the solidification direction are observable in all samples. However, the cell spacing (λ) varies depending on *E*, i.e., λ decreases from 0.78 ± 0.07 μm to 0.54 ± 0.06 μm with decreasing *E* (Fig. 3 (d)). Fig. 4 (a) and (b) show TEM-bright field (BF) images of the cells in the sub-layer of HE sample in terms of the SD and BD, respectively. Numerous dislocations are tangled in the form of a cylinder-like dislocation cell parallel to BD. It should be noted that the spacing between the dislocation cells is approximately 0.8 μm and the value is generally consistent with λ observed by SEM-BSE (Fig. 3). Fig. 4 (c)–(e) show selected area electron diffraction (SAED) patterns obtained from points highlighted by white circles in Fig. 4 (b). Note that the beam directions in all these SAED patterns were set parallel to [001] at area (c). Therefore, the slight deviations of diffraction patterns observed at areas (d) and (e) indicate that there are several degrees of crystallographic misorientation between neighboring cells. As shown in Fig. 4 (e), the cell at (e) is rotated with several degrees (≈2°) of misorientation compared with that at (c). These results indicate that the boundaries of cells are low angle grain boundaries (LAGBs), which exhibit one or both of tilting and twisting misorientations between adjacent cells. Fig. 5 shows STEM-high-angle annular dark field (HAADF) image (a) and STEM-energy dispersive spectroscopy (EDS) maps (b)–(f) of the cells in the sub-layer

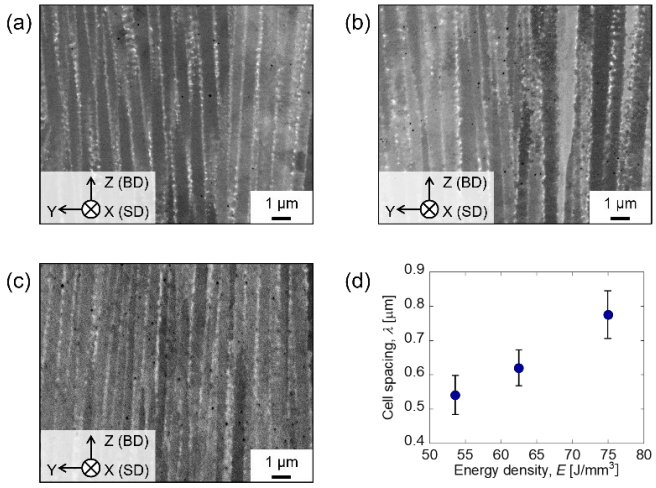

Fig. 3 Cells of the sub-layer in HE (a), ME (b) and LE (c) rods taken from SD. (d) Variations in λ as a function of *E*.

of HE sample taken from the BD. As shown in Fig. 5 (a), the dislocation cell at the cell boundary has a wall-like morphology, with a width of approximately 200 nm. Furthermore, the elemental distribution maps (Fig. 5 (b)–(f)) clearly show that concentration of Nb and Ti are enhanced in the dislocation cell wall. These findings indicate that the cells are formed by dendritic solidification with super-rapid cooling rate (~10^7 K/s) [14]. The secondary arms, one of the characteristics of the dendritic structure, are difficult to grow during SLM fabricating due to the super-rapid cooling, resulting in the formation of the columnar cells. Furthermore, a decrease in E leads to a further increase in the cooling rate, which reduces the cell spacing. Nevertheless, it is challenging to provide a comprehensive explanation for the formation of the dislocation cell wall in exclusively dendritic solidification terms. In the SLM process, a large residual stress is formed due to super-rapid cooling. This residual stress exceeding the yield stress of the alloy results in strain relaxation to introduce numerous dislocations. It should be noted that the solid solution strengthening of the segregation area is stronger than that of the cell interior due to high Nb and Ti concentrations. Thus, the dislocations accumulate in the segregation area and form the dislocation cell wall. The tensile strength of the alloy is significantly affected by these unique cells.

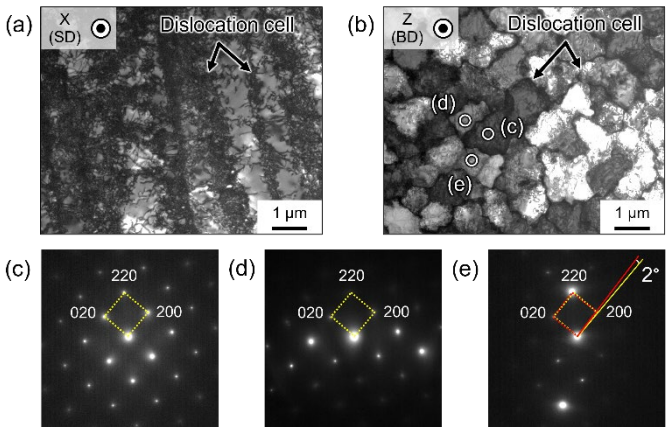

Fig. 4 The cells in sub-layer of HE rod in terms of SD (a) and BD (b). (c)–(e) SAED patterns obtained from the region marked by white circles in (b).

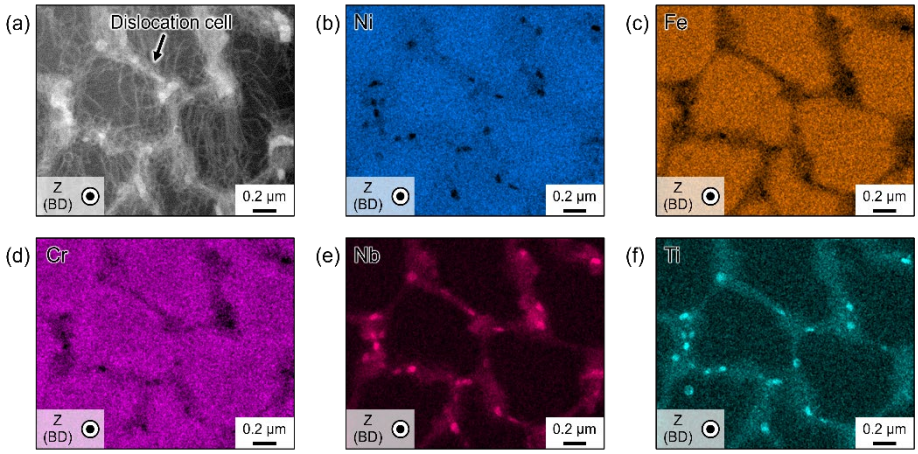

Fig. 5 The distribution of dislocation cell (a) and segregations (b)-(f) of cells in the sub-layer of HE sample taken from the BD. (b) Ni, (c) Fe, (d) Cr, (e) Nb and (f) Ti.

Tensile properties. The yield stresses ($\sigma_{0.2}$) of Inconel 718 samples having unique hierarchical structure manufactured via SLM with different E are listed in Table 2. $\sigma_{0.2}$ of the samples increases from 539 ± 2 MPa to 560 ± 3 MPa with decreasing E. Note that there are no obvious differences in the crystallographic orientation and width of CLM of these samples. Thus, the difference in strength can be attributed to variations in the morphology of the cells. Fig. 6 shows the relationship between $\sigma_{0.2}$ and $\lambda^{-1/2}$. It is obvious that there is Hall-Petch relationship between $\sigma_{0.2}$ and λ, as expressed in Eq. 2,

$$\sigma_{0.2} = \sigma_0 + k\lambda^{-1/2}. \quad (2)$$

where σ_0 and k represent the yield stress of the samples in the absence of cells and the Hall-Petch coefficient, respectively. Such agreement with Hall-Petch relationship suggests that the boundary of the cells consisting of a LAGB accompanied with dislocation cell wall and segregation area performs as a significant obstacle to the motion of griding dislocations like refinement strengthening following Hall-Petch relationship. In other words, the mobile dislocations cannot pass through the boundary of cells and accumulate outside of the boundary. In fact, the value of k (92 MPa·μm$^{-1/2}$) is comparable to or higher than that reported for a high angle grain boundary (HAGB) in polycrystalline pure Ni (68 MPa·μm$^{-1/2}$) [15].

Table 2 Yield stress $\sigma_{0.2}$ of each rod.

	Yield stress [MPa]
HE rod	539 ± 2
ME rod	548 ± 3
LE rod	560 ± 3

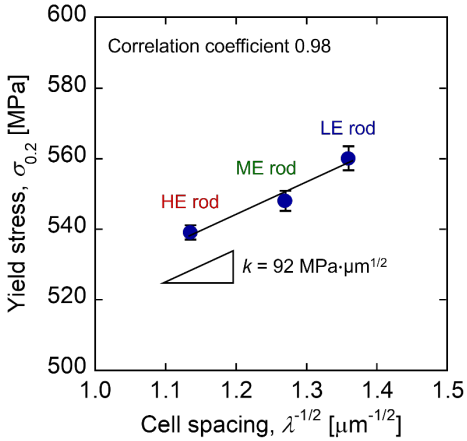

Fig. 6 Reletionship between $\sigma_{0.2}$ and $\lambda^{-1/2}$.

Summary

The morphology of cells and its effect on tensile strength of Inconel 718 having unique hierarchical structure manufactured via SLM were examined focusing on the input energy density. The following findings were derived from the present work:

1. The boundary of cells is LAGB coexisting with dislocation cell wall and segregation of Nb and Ti. The formation of the cells is resulted from the dendric solidification and subsequent stress relaxation.
2. The cell spacing decreases with decreasing E. This phenomenon can be attributed to the increase in the cooling rate, which occurs in conjunction with a decrease in E.
3. Although the boundary of cells is a LAGB, significant refinement strengthening according to Hall-Petch relationship comparable to or higher than that attributed to a HAGB can be obtained. This is because the boundary of cells performs as a pile-up site for the griding dislocation.

Acknowledgement

This work was supported by CREST-Nanomechanics: Elucidation of macroscale mechanical properties based on understanding nanoscale dynamics of innovative mechanical materials (Grant Number: JPMJCR2194) from the Japan Science and Technology Agency (JST).

References

[1] T. Sonar, V. Balasubramanian, S. Malarvizhi, T. Venkateswaran, D. Sivakumar, An overview on welding of Inconel 718 alloy - Effect of welding processes on microstructural evolution and mechanical properties of joints, Mater. Charact. 174 (2021) 110997.

[2] P.M. Mignanelli, N.G. Jones, E.J. Pickering, O.M.D.M. Messé, C.M.F. Rae, M.C. Hardy, H.J. Stone, Gamma-gamma prime-gamma double prime dual-superlattice superalloys, Scr. Mater. 136 (2017) 136–140.

[3] J.J.J. Shi, X. Li, Z.X.X. Zhang, G.H.H. Cao, A.M.M. Russell, Z.J.J. Zhou, C.P.P. Li, G.F.F. Chen, Study on the microstructure and creep behavior of Inconel 718 superalloy fabricated by selective laser melting, Mater. Sci. Eng. A 765 (2019) 138282.

[4] J.C. Colombo-Pulgarín, C.A. Biffi, M. Vedani, D. Celentano, A. Sánchez-Egea, A.D. Boccardo, J.-P. Ponthot, Beta Titanium Alloys Processed By Laser Powder Bed Fusion: A Review, J. Mater. Eng. Perform. 30 (2021) 6365–6388.

[5] W. Yang, M. Li, S. Su, S. Xiao, Y. Chen, Effects of carbon addition on the microstructure and mechanical property of in-situ reinforced TiAl matrix composite powders produced by plasma rotating electrode process, J. Mater. Res. Technol. 27 (2023) 5204–5218.

[6] Y. Luo, S. Liu, Z. Sun, B. Liu, L. Wang, Y. Wang, Y. Liu, Microstructural evolution during annealing of a powder metallurgical TiAl–Nb composite and its effect on mechanical properties, J. Mater. Res. Technol. 25 (2023) 3654–3669.

[7] H. Gong, K. Rafi, H. Gu, T. Starr, B. Stucker, Analysis of defect generation in Ti–6Al–4V parts made using powder bed fusion additive manufacturing processes, Addit. Manuf. 1–4 (2014) 87–98.

[8] B. Vayssette, N. Saintier, C. Brugger, M. El May, Surface roughness effect of SLM and EBM Ti-6Al-4V on multiaxial high cycle fatigue, Theor. Appl. Fract. Mech. 108 (2020).

[9] G. Sander, A.P. Babu, X. Gao, D. Jiang, N. Birbilis, On the effect of build orientation and residual stress on the corrosion of 316L stainless steel prepared by selective laser melting, Corros. Sci. 179 (2021).

[10] Y. Song, Q. Sun, K. Guo, X. Wang, J. Liu, J. Sun, Effect of scanning strategies on the microstructure and mechanical behavior of 316L stainless steel fabricated by selective laser melting, Mater. Sci. Eng. A 793 (2020) 1–7.

[11] D. Zhang, Z. Feng, C. Wang, W. Wang, Z. Liu, W. Niu, Comparison of microstructures and mechanical properties of Inconel 718 alloy processed by selective laser melting and casting, Mater. Sci. Eng. A 724 (2018) 357–367.

[12] T.D. McLouth, G.E. Bean, D.B. Witkin, S.D. Sitzman, P.M. Adams, D.N. Patel, W. Park, J.M. Yang, R.J. Zaldivar, The effect of laser focus shift on microstructural variation of Inconel 718 produced by selective laser melting, Mater. Des. 149 (2018) 205–213.

[13] O. Gokcekaya, T. Ishimoto, S. Hibino, J. Yasutomi, T. Narushima, T. Nakano, Unique crystallographic texture formation in Inconel 718 by laser powder bed fusion and its effect on mechanical anisotropy, Acta Mater. 212 (2021) 116876.

[14] M. Okugawa, K. Saito, H. Yoshima, K. Sawaizumi, S. Nomoto, M. Watanabe, T. Nakano, Y. Koizumi, Solute segregation in a rapidly solidified Hastelloy-X Ni-based superalloy during laser powder bed fusion investigated by phase-field and computational thermal-fluid dynamics simulations, Addit. Manuf. 84 (2024) 104079.

[15] C. Keller, E. Hug, Hall-Petch behaviour of Ni polycrystals with a few grains per thickness, Mater. Lett. 62 (2008) 1718–1720.